

# Simulation of Particulate Fouling and its Influence on Friction Loss and Heat Transfer on Structured Surfaces using Phase-Changing Mechanism



Robert Kasper, Johann Turnow and Nikolai Kornev

**Abstract** Numerical simulations of particulate fouling using highly resolved Large-Eddy Simulations (LES) are carried out for a turbulent flow through a smooth channel with a single spherical dimple or square cavity (dimple depth/cavity depth to dimple diameter/cavity side length ratio of  $t/D = 0.261$ ) at  $Re_D = 42,000$ . Therefore, a new multiphase method for the prediction of particulate fouling on structured heat transfer surfaces is introduced into OpenFOAM<sup>®</sup> and further described. The proposed method is based on a combination of the Lagrangian Particle Tracking (LPT) and Eulerian approaches. Suspended particles are simulated according to their natural behavior by means of LPT as solid particles, whereas the carrier phase is simulated using the Eulerian approach. The first numerical results obtained from LES approve the capabilities of the proposed method and reveal a superior fouling performance of the spherical dimple due to asymmetric vortex structures, compared to the square cavity.

## 1 Introduction

The common way to evaluate the performance of heat transfer enhancement methods like ribs, fins, or dimples is the determination of the thermo-hydraulic efficiency, which is the relationship of the increased heat exchange to pressure loss [1]. Despite the fact that particulate fouling, the accumulation of particles on the heat transfer surfaces, reduces thermo-hydraulic performance significantly, an universal method for the prediction of particulate fouling still does not exist. With respect to the large time instants and variety of fouling, its influence is mainly determined using experimental investigations. Due to improved numerical algorithms and access to high computational resources, numerical simulations of fouling have become more and more advantageous. However, commonly used fouling models are derived for a

---

R. Kasper · J. Turnow (✉) · N. Kornev  
Chair of Modeling and Simulation, University of Rostock,  
Albert-Einstein-Str. 2, 18059 Rostock, Germany  
e-mail: [johann.turnow@uni-rostock.de](mailto:johann.turnow@uni-rostock.de)

R. Kasper  
e-mail: [robert.kasper@uni-rostock.de](mailto:robert.kasper@uni-rostock.de)

© Springer Nature Switzerland AG 2019  
J. M. Nóbrega and H. Jasak (eds.), *OpenFOAM*<sup>®</sup>,  
[https://doi.org/10.1007/978-3-319-60846-4\\_31](https://doi.org/10.1007/978-3-319-60846-4_31)

definite set of boundary conditions and are calibrated for specific cases [2]. Hence, the existing fouling approaches are unsuitable for a general prediction and analysis of particulate fouling for industrial applications. Within the present work, a new approach has been introduced to determine the local fouling layer growth and its influence on heat transfer and pressure loss. Numerical simulations using different existing fouling algorithms have shown that the efficiency of the numerical simulations depend enormously on the fouling model used and its empirical parameters, in combination with the complexity of the heat transfer surface. To reduce computational time and increase the universality of the model, the proposed method was developed based on Lagrangian Particle Tracking (LPT) and the Euler approach, in which the deposited particles are transferred into an extra fouling layer phase with predefined material properties, causing additional friction losses and heat transfer resistance. The vortex formations and their direct impact on fouling probability, and thus on the heat transfer for a single spherical dimple and rectangular cavity, are analyzed and compared to results obtained for a clean surface.

## **2 Multiphase Approach for the Simulation of Particulate Fouling**

The numerical simulation of particulate fouling on heat transfer surfaces is complex, consisting mainly of the deposition of small particles due to adhesion and sedimentation of larger particles resulting from gravitational forces. Therefore, the proposed multiphase method for the simulation of particulate fouling is composed of two different branches that are closely related to each other. The first one is the Lagrangian branch and describes the physics of the suspended particles or, respectively, the dispersed phase using the LPT. This branch is mainly responsible for the transport of the particles to the heat transfer surfaces, the deposition of the particles due to adhesion and sedimentation, and also the resuspension of deposited particles due to local shear stresses. The second one is the Eulerian branch and determines the flow fields of the carrier flow (i.e., the continuous phase) with respect to the settled fouling layer, which are then again required within the Lagrangian branch.

### ***2.1 Lagrangian Branch***

The description of particle motions within a fluid using the Lagrangian Particle Tracking (LPT) requires the solution of the following set of ordinary differential equations along the particle trajectory, which enables the calculation of the particle location and the linear, as well as the angular, particle velocity at anytime:

$$\frac{d\mathbf{x}_p}{dt} = \mathbf{u}_p, \quad (1)$$

$$m_p \frac{d\mathbf{u}_p}{dt} = \sum \mathbf{F}_i, \quad (2)$$

$$I_p \frac{d\boldsymbol{\omega}_p}{dt} = \sum \mathbf{T}, \quad (3)$$

where  $m_p = \pi/6\rho_p D_p^3$  is the particle mass,  $I_p = 0.1m_p D_p^2$  is the moment of inertia (for a sphere),  $\mathbf{F}_i$  includes all the relevant forces acting on the particle, and  $\mathbf{T}$  is the torque acting on a rotating particle due to viscous interaction with the carrier fluid [3]. Equation (2) represents Newton's second law of motion and presupposes the consideration of all relevant forces acting (drag, gravity and pressure forces) on the particle

$$m_p \frac{d\mathbf{u}_p}{dt} = \sum \mathbf{F}_i = \mathbf{F}_D + \mathbf{F}_G + \mathbf{F}_P + \dots \quad (4)$$

However, analytical solutions for different forces exists only for small particle Reynolds numbers, respectively, for the Stokes regime [4]. Due to the fact that the consideration of intermediate and high particle Reynolds numbers is also desirable, the LPT used in this work is extended to a wide range of particle Reynolds numbers. The implemented drag model is based on the particle Reynolds number, which is defined as

$$\text{Re}_p = \frac{\rho_f D_p |\mathbf{u}_f - \mathbf{u}_p|}{\mu_f}, \quad (5)$$

with the density  $\rho_f$  and the dynamic viscosity  $\mu_f$  of the fluid or continuous phase, the particle diameter  $D_p$  and the difference between flow and particle velocity  $|\mathbf{u}_f - \mathbf{u}_p|$ . The drag coefficient is now determined, based on the particle Reynolds number, through the following empirical relation proposed by Putnam [5]:

$$C_D \text{Re}_p = \begin{cases} 24 \left(1 + \frac{1}{6} \text{Re}_p^{2/3}\right) & \text{if } \text{Re}_p \leq 1000 \\ 0.424 \text{Re}_p & \text{if } \text{Re}_p > 1000. \end{cases} \quad (6)$$

After determination of the drag coefficient, the basic equation of motion for a spherical particle is used to evaluate the drag force

$$\mathbf{F}_D = C_D \frac{\pi D_p^2}{8} \rho_f (\mathbf{u}_f - \mathbf{u}_p) |\mathbf{u}_f - \mathbf{u}_p|. \quad (7)$$

In addition to the drag force, the gravitational and buoyancy force and the pressure gradient force have to be taken into account as well. Within the LPT used, gravitation and buoyancy are computed as one total force as follows:

$$\mathbf{F}_G = m_p \mathbf{g} \left(1 - \frac{\rho_f}{\rho_p}\right), \quad (8)$$

where  $\mathbf{g}$  is the gravitational acceleration vector. The resultant force due to a local fluid pressure gradient acting on a spherical particle can be found from Eq. (9) using the differential form of the momentum equation to express the pressure gradient:

$$\mathbf{F}_P = \rho_f \frac{\pi D_p^3}{6} \left( \frac{D\mathbf{u}_f}{Dt} - \nabla \cdot \nu_f (\nabla \mathbf{u}_f + \nabla \mathbf{u}_f^T) \right). \quad (9)$$

From Newton's third law of motion, it follows that if a particle is either accelerated or decelerated in a fluid, an accelerating or decelerating of a certain amount of the fluid surrounding the particle is required. This additional force is known as added mass force, sometimes referred to as virtual mass force, and can be expressed as

$$\mathbf{F}_A = C_A \rho_f \frac{\pi D_p^3}{6} \left( \frac{D\mathbf{u}_f}{Dt} - \frac{d\mathbf{u}_p}{dt} \right), \quad (10)$$

where  $C_A$  is the so-called added mass coefficient. This coefficient can be exactly derived for spherical particles from potential theory and is  $C_A = 1/2$ .

The last considered force arises due to local shear flows, and therefore from a nonuniform velocity distribution over the particle surface. This lift force is called the Saffman force and is modeled using the Saffman-Mei model, derived by Saffman [6, 7] and advanced by Mei [8]. In order to determine the lift force due to local shear flows, the shear Reynolds number has to be calculated

$$\text{Re}_s = \frac{\rho_f D_p^2 |\nabla \times \mathbf{u}_f|}{\mu_f}, \quad (11)$$

which is used to evaluate the coefficients of the Saffman-Mei model

$$\beta = \frac{1}{2} \frac{\text{Re}_s}{\text{Re}_p}, \quad \alpha = 0.3314\sqrt{\beta}, \quad f = (1 - \alpha) \exp(-0.1\text{Re}_p) + \alpha. \quad (12)$$

Afterward, the lift coefficient  $C_{LS}$  is calculated using the following approximation:

$$C_{LS} = \begin{cases} 6.46 f & \text{if } \text{Re}_p < 40 \\ 6.46 \cdot 0.0524\sqrt{\beta\text{Re}_p} & \text{if } \text{Re}_p \geq 40. \end{cases} \quad (13)$$

The lift coefficient  $C_{LS}$  is now expressed in terms of a nondimensional lift coefficient

$$C_L = \frac{3}{2\pi\sqrt{\text{Re}_s}} C_{LS}. \quad (14)$$

This conversion allows for a more universal way of determining the lift force using any conceivable force model. Finally, the lift force is calculated as

$$\mathbf{F}_L = C_L \rho_f \frac{\pi D_p^3}{6} (\mathbf{u}_f - \mathbf{u}_p) \times (\nabla \times \mathbf{u}_f). \quad (15)$$

In summary, it can be stated that the proposed LPT is capable of considering the most important forces acting on a particle. Because numerical simulations of Sommerfeld have shown that the consideration of the Basset force increases the computational time by a factor of about 10 [3], this force is neglected. This strategy is valid for small density ratios  $\rho_f/\rho_p \ll 1$  [4], which is probably not the case for liquid-solid flows, as investigated below. Thus, the influence of the Basset force has to be analyzed in the future.

However, another important concept in the analysis of dispersed multiphase flows is phase coupling. One-way coupling exists if the carrier flow effects the particles while there is no reverse effect. If there is a mutual effect between carrier flow and particles, then the flow is two-way coupled [4]. In the case of dense flows, there will be an additional interaction among the particles themselves, which is what is meant by four-way coupling. The proposed method is capable of considering all different types of coupling.

### 2.1.1 Deposition of Particles

As already mentioned, the proposed method has to include an algorithm for the physical modeling of the deposition of suspended particles on solid walls or, more precisely, on heat transfer surfaces. Due to the fact that particle deposition is mainly caused by particle–wall adhesion within this work, the implemented model is based on the suggestions of Löffler and Muhr [9] and, furthermore, Heinel and Bohnet [10]. This model consists of an energy balance around the particle–wall and particle–fouling collision. Thus, a critical particle velocity can be derived from a local energy balance, which contains the kinetic energy before and after the collision, the energy ratio describing the adhesion due to van der Waals forces and a specific amount considering the energy loss of a particle resulting from particle–wall and particle–fouling collision. From the condition of adhesion (i.e., a particle is not able release itself from the wall after the collision), the critical particle velocity yields

$$u_{p,\text{crit}} = \sqrt{\left(\frac{\hbar\varpi}{eD_p 4\pi^2 z_0^2}\right)^2 \frac{3}{4H\rho_p}}, \quad (16)$$

where  $\hbar\varpi$  is the Lifschitz–van der Waals energy,  $z_0$  is the distance at contact,  $H$  is the strength of the contact wall, and  $e$  is the coefficient of restitution. It should be mentioned at this point that the determination of the critical particle velocity (16) can be easily extended for the consideration of electrostatic forces [9, 10]. However, the condition of adhesion is achieved, if the particle velocity before the wall collision (impact velocity) is smaller than the critical particle velocity

$$|\mathbf{u}_p| \leq u_{p,\text{crit}}. \quad (17)$$

To increase the computational efficiency of our proposed method, particles that fulfill the adhesion condition, Eq. (17), are converted into an additional continuous/solid phase (fouling layer) and will be deactivated within the LPT. Thus, the amount of particles is kept nearly constant during the calculations, which reduces the computational time enormously. The initiated volume or phase fraction  $\alpha$  is evaluated by the particle volume with respect to the cell volume

$$\alpha_{new,i} = \alpha_{old,i} + \frac{V_p}{V_i}, \tag{18}$$

where  $\alpha_{old,i}$  is the phase fraction from the previous time step and  $V_p$  and  $V_i$  are the particle and cell volume, respectively. Figure 1 shows the basic concept of the implemented phase conversion algorithm. According to this, it can be distinguished between two different cases if a deposited particle has to be converted into the fouling phase. If the residual local cell volume is greater than the particle volume, the new phase fraction  $\alpha$  can be simply determined using Eq. (18). If the remaining local cell volume is smaller than the particle volume, the phase fraction is allocated to the neighbor cell with the maximum cell-based phase fraction gradient  $\max(\nabla\alpha)$ . Hence, the neighbor cell with the lowest phase fraction is filled with the fouling phase. To consider the influence of the fouling phase, an additional porosity source term (based on Darcy’s law)

$$\mathbf{S}_p = \alpha \frac{\mu_f}{K} \mathbf{u}_f, \tag{19}$$

has been introduced into the momentum balance equation, where  $K$  is the permeability of the fouling phase. Thus, the blocking effect or flow section contraction due to deposited particles is not explicitly considered within the calculations, but rather is modeled implicitly in terms of a porous fouling layer. Furthermore, any physical property  $x_i$  (e.g., density, dynamic/kinematic viscosity, or thermal diffusivity) for partially filled cells is interpolated as follows:

$$x_i = \alpha \cdot x_{fouling} + (1 - \alpha) \cdot x_{fluid}, \tag{20}$$

whereas, the physical properties of the carrier fluid are fully applied at cells without the fouling phase ( $\alpha = 0$ ) and cells that are completely occupied by the fouling phase ( $\alpha = 1$ ) take the physical properties of the fouling material. This procedure likewise

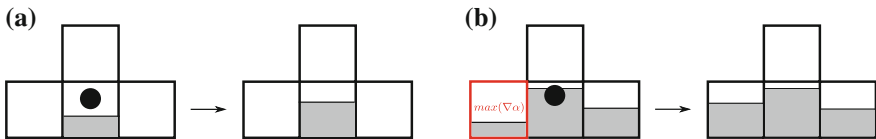


**Fig. 1** Basic mechanism of the phase conversion algorithm: **a**  $V_c > V_p$  and **b**  $V_c < V_p$

allows for evaluation of the heat transfer under consideration of particulate fouling and prevents the solving of an additional advection/transport equation for the fouling phase, as well as the application of costly remeshing procedures.

### 2.1.2 Resuspension of Deposited Particles

The resuspension of deposited particles (i.e., the release of particles from the fouling layer and re-entrainment into the carrier fluid due to high local shear stresses) is an important mechanism, which has to be considered in the proposed approach to simulate the particulate fouling as accurately as possible. Therefore, a simple resuspension model is derived based on the Kern and Seaton model [2]

$$\alpha_{removed} = \min\left(\frac{V_p}{\tau_{rel}} \frac{|\tau_c|}{V_c}, \frac{V_p}{V_c}\right), \quad (21)$$

where  $\tau_{rel}$  is a relative shear stress and  $\tau_c$  is the cell-based local shear stress. The relative shear stress has to be measured in experiments and can be interpreted as a threshold value for the release of fouling volume due to high local shear stresses. The number of resuspended (spherical) particles can be determined using the definition of the sphere volume

$$n = \frac{\alpha_{removed} V_c}{\pi D_p^3/6}. \quad (22)$$

The resuspended particles will be re-activated and become part of the LPT again, whereby the initial momentum and forces are calculated according to the force models described above.

## 2.2 Eulerian Branch

The governing equations are the incompressible Navier–Stokes equations (extended by the porosity source term  $\mathbf{S}_p$ , which takes the influence of the fouling layer into account), the continuity equation and a passive scalar transport equation for the temperature. This system of partial differential equations is solved numerically using OpenFOAM®. Although the turbulence modeling is generic, Large-Eddy Simulations (LES) are carried out to investigate the interaction between local vortex structures and particulate fouling. LES is a widely used technique for simulating turbulent flows and allows one to explicitly solve for the large eddies and implicitly account for the small eddies by using a Subgrid-Scale model (SGS model).

### 2.2.1 Large-Eddy Simulation

The LES equations are derived by filtering the continuity equation, the Navier–Stokes equations and the passive scalar transport equation for the temperature using an implicit box filter with a filter width  $\bar{\Delta}$  (depending on the computational grid):

$$\nabla \cdot \bar{\mathbf{u}} = 0, \tag{23}$$

$$\frac{\partial \bar{\mathbf{u}}}{\partial t} + \nabla \cdot (\bar{\mathbf{u}} \bar{\mathbf{u}}) = -\frac{1}{\rho} \nabla p + \nabla \cdot \nu (\nabla \bar{\mathbf{u}} + \nabla \bar{\mathbf{u}}^T) + \nabla \cdot \boldsymbol{\tau}_{SGS} - \bar{\mathbf{S}}_p, \tag{24}$$

$$\frac{\partial \bar{T}}{\partial t} + \nabla \cdot (\bar{\mathbf{u}} \bar{T}) = \nabla \cdot \left( \frac{\nu(\alpha)}{\text{Pr}(\alpha)} \nabla \bar{T} \right) + \nabla \cdot \mathbf{J}_{SGS}. \tag{25}$$

The unclosed subgrid-scale stress tensor  $\boldsymbol{\tau}_{SGS} = \overline{\mathbf{u}\mathbf{u}} - \bar{\mathbf{u}}\bar{\mathbf{u}}$  is modeled using a dynamic one-equation eddy viscosity model proposed by Yoshizawa and Horiuti [11] and Kim and Menon [12]. This SGS model uses a modeled balance equation to simulate the behavior of the subgrid-scale kinetic energy  $k_{SGS}$  in which the dynamic procedure of Germano et al. [13] is applied to evaluate all required coefficients dynamically in space and time. The subgrid-scale scalar flux  $\mathbf{J}_{SGS}$  [see Eq. (25)] can be considered using a gradient diffusion approach.

### 2.3 Computational Grid and Boundary Conditions

For the simulation of particulate fouling on structured surfaces, two academical test-cases, a smooth channel with a single square cavity and one with a spherical dimple, have been investigated. The computational domain for both testcases is shown in Fig. 2. The origin of the coordinate system is located in the center of the dimple, respectively, the cavity, and is projected onto the lower wall plane, therefore the

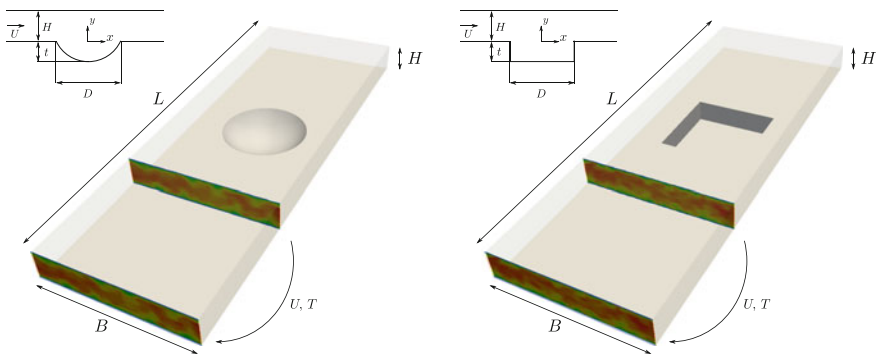


**Fig. 2** Computational domain for a smooth channel with a single spherical dimple (left) and a square cavity (right)



lower wall is located at  $y/H = 0.0$ . The length of the channel is  $L = 230$  mm, while channel height  $H$  and channel width  $B$  are set to  $H = 15$  mm and  $B = 80$  mm. For the spherical dimple with a sharp edge, a diameter of  $D = 46$  mm and a dimple depth  $t = 12$  mm are chosen, while the side length of the square cavity equals the dimple diameter  $D$  and the cavity depth is likewise set to  $t = 12$  mm. Periodic boundary conditions were applied in the spanwise direction, whereas no slip boundary conditions were set at the lower and upper channel walls. Turbulent inlet conditions were produced using a precursor method, which copies the turbulent velocity and temperature field from a plane downstream the channel entrance back onto the inlet. The nondimensionalized form of the temperature

$$T^+ = \frac{T - T_\infty}{T_w - T_\infty} \quad (26)$$

is used, where a constant  $T^+ = 1$  is assumed at the lower wall. The molecular Prandtl number was set to be  $Pr = 0.71$ , whereas the turbulent Prandtl number  $Pr_t$  was 0.9 in all simulations. The Reynolds number based on the averaged bulk velocity  $U_b$  and the dimple diameter, respectively the cavity side length  $D$ , was equal to  $Re_D = 42,000$ . To assure grid independence of the obtained results, a series of calculations on different grid resolutions was carried out. Therefore, block-structured curvilinear grids consisting of around  $7.8 \times 10^5$ ,  $1.6 \times 10^6$  and  $3.3 \times 10^6$  cells were used. In the spanwise and streamwise direction, an equidistant grid spacing is applied, whereas in the wall-normal direction, a homogeneous grid stretching is used to place the first grid node inside of the laminar sublayer at  $y^+ \approx 1$ . Spherical monodisperse quartz particles ( $SiO_2$ ) with a diameter of  $D_p = 20 \mu m$  are randomly injected within the flow inlet for the fouling simulations. Based on an earlier experimental fouling investigation [14], a total particle mass up to  $m_p \approx 5.5$  g/s is chosen to ensure an asymptotic fouling layer growth against a limit value within a few minutes of physical realtime. The estimated volume fraction of the dispersed phase is  $\alpha_d < 0.001$ , which corresponds to a dilute flow and allows for the negligence of particle collisions [4]. Hence, only two-way coupling is considered during the simulations.

## 3 Results

### 3.1 Validation

The functionality and accuracy of our proposed method, as well the Lagrangian Particle Tracking, as the simulation of a fully turbulent flow in a smooth channel with a single spherical dimple at  $Re_D = 42,000$  is validated within this section.

### 3.1.1 Lagrangian Particle Tracking

The Taylor–Green vortex flow is chosen to investigate the performance of the implemented Lagrangian Particle Tracking (LPT). This flow is selected due to the existence of its exact solution of the corresponding instantaneous velocity field and streamfunction as a special case of a two-dimensional time-dependent solution to the Navier–Stokes equations. The two-dimensional Taylor–Green vortex is assumed to be in the  $x$ - $y$ -plane, and the flow is uniform in the  $z$ -direction. Therefore, the instantaneous local streamfunction can be written as [15]

$$\Psi(x, y, t) = \frac{\omega_0}{k^2} \cos(k_x x) \cos(k_y y) \exp(-\text{Re}_0^{-1} k^2 t), \quad (27)$$

where the corresponding instantaneous fluid velocity components can be directly derived from Eq. (27)

$$u_x = \frac{\partial \Psi}{\partial y} = -\omega_0 \frac{k_y}{k^2} \cos(k_x x) \sin(k_y y) \exp(-\text{Re}_0^{-1} k^2 t), \quad (28)$$

$$u_y = -\frac{\partial \Psi}{\partial x} = \omega_0 \frac{k_x}{k^2} \sin(k_x x) \cos(k_y y) \exp(-\text{Re}_0^{-1} k^2 t), \quad (29)$$

where  $\omega_0$  is the initial vorticity maximum,  $k_x$  and  $k_y$  are the wave numbers in the  $x$ - and  $y$ -directions and  $k^2 = k_x^2 + k_y^2$ . It is assumed that the gravitational acceleration is normal to the flow plane ( $x - y$ ), so that it does not affect the particle dynamics. The simulations are performed with the following parameters:  $\text{Re}_0^{-1} = 0.004$ ,  $k_x = k_y = 1$ ,  $\omega_0 = 2$ ,  $x$  and  $y$  are in the range of 0 and  $2\pi$ . Spherical particles with a constant diameter of  $D_p = 0.001$  m were randomly seeded within the flow field.

The primary objective of this testcase is to examine the effects of the so-called momentum (velocity) response time

$$\tau_V = \frac{\rho_p D_p^2}{18\mu_f} \quad (30)$$

with respect to the particle trajectories, which exemplifies the functionality of the implemented Lagrangian Particle Tracking in a qualitative manner. The momentum response time relates to the time required for a particle to respond to a change in velocity [4]. For the case of nearly massless particles ( $\tau_V \approx 0$ ), the particle trajectories should follow the flow streamlines exactly. For the case of heavier particles ( $\tau_V > 0$ ), their trajectories are expected to deviate from the flow streamlines due to inertial effects. Therefore, only the drag force is considered within the simulations. Fig. 3 compares the particle trajectories after simulating 3.4 s of physical real time for different momentum response times to the streamlines of the two-dimensional Taylor–Green vortex computed from the stream function Eq. (27).

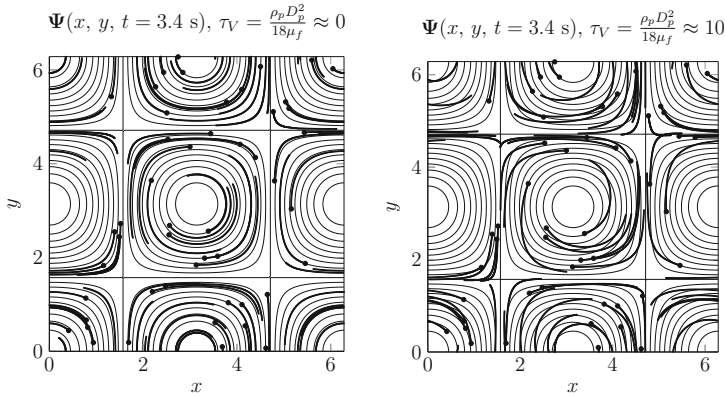


**Fig. 3** Two-dimensional Taylor–Green vortex: streamlines (contour lines) and particle trajectories (thick dotted lines) for  $\tau_V \approx 0$  (left) and  $\tau_V \approx 10$  (right); thick dots represents the initial positions of the randomly seeded particles

It is obvious that the motion of the particles seems to be correctly described by the LPT, because the fluid particles in the case of  $\tau_V$  follows the streamlines very well. With increasing particle response time  $\tau_V$ , the particles get their own inertia and they lose the ability to follow the carrier flow. As expected, other numerical results shows that a step-wise increase of the particle response times  $\tau_V$  leads to a step-wise increased deviation of the particle trajectories from the flow streamlines. The obtained results confirms that the implemented LPT routines are capable of describing the motion of the particles correctly.

### 3.1.2 Flow in a Smooth Channel with a Single Spherical Dimple

Numerical results for a smooth channel with a single spherical dimple are validated using experimental data published by Terekhov et al. [16] and Turnow et al. [17]. Figure 4 shows the profile of the normalized mean velocity  $\langle U \rangle / U_0$  and Reynolds stress  $\langle U_{rms} \rangle / U_0$  in the flow direction received from URANS ( $k-\omega$ -SST model with a fine grid; for comparative purposes only) and LES for three different grid resolutions and from LDA measurements along the  $y$ -axis at  $x/D = 0.0$  and  $z/H = 0.0$  (center of the dimple). The numerical results are obtained for Reynolds number  $Re_D = 42,000$  and are normalized by the maximum velocity  $U_0$  in the center of the channel at  $y = H/2$ . A satisfactory overall agreement of calculated and measured mean velocity profiles has been obtained for all three grid resolutions. The mean velocity profiles from LES and URANS matches well with the measurements in the center of the channel where the maximum flow velocity occurs, and even in the upper near wall region. However, slight deviations from the measured profiles can be registered for both methods and all grid resolutions inside of the spherical dimple within the distinct recirculation zone. Nevertheless, since URANS and LES results are in good

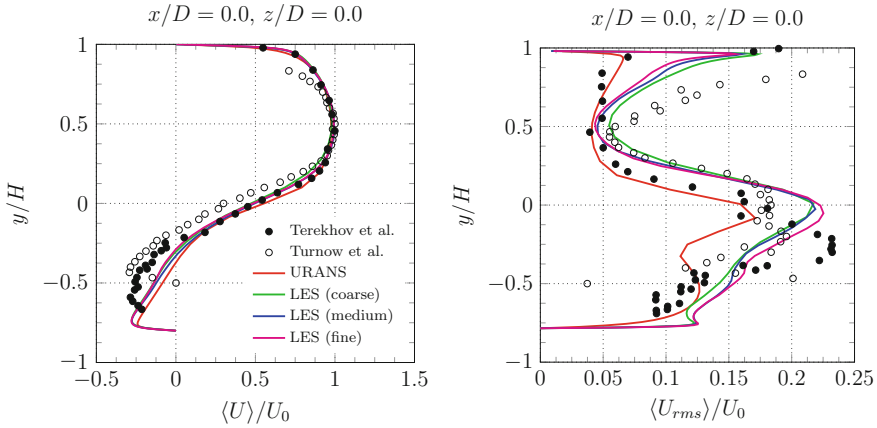


**Fig. 4** Mean velocity and Reynolds stress profiles obtained from URANS and LES in comparison with experiments by Terekhov et al. and Turnow et al.

agreement in this region, the likeliest reason for the discrepancy between measurements and calculations might be LDA measurement problems in close proximity to the wall [17]. From the mean velocity profiles, one can observe, that the strongest velocity gradients arises at the level of the lower channel wall  $y/H = 0.0$ . The instabilities of the shear layer within this region result in strong vortices, and therefore in high Reynolds stresses, which can be observed in all Reynolds stress profiles. Unlike the mean velocity profiles, the level of the Reynolds stresses and, furthermore, the location of the maximum turbulent fluctuations measured in experiments can only be gained using LES. A deviation between the measured and calculated locations of the maximum Reynolds stresses are notable within the center of the dimple at position  $x/D = 0.0$ . The weakness of URANS is clearly visible in the near wall region and the level of the lower wall, where the magnitude of the turbulent fluctuations can not be captured. Due to the significant importance of the resolved Reynolds stresses for calculating the resuspension rate of deposited particles (see Sect. 2.1.2), URANS seems to be inappropriate for further investigations.

Probably the most important feature of the investigated spherical dimple with a dimple depth to dimple diameter ratio of  $t/D = 0.261$  can be observed from the phase averaged streamline pattern given in Fig. 5. The streamlines shows unsteady asymmetrical monocore vortex structures inside the dimple, which switches their orientation arbitrarily from  $\alpha = -45^\circ$  to  $\alpha = +45^\circ$  with respect to the main flow direction. The existence of long period self-sustained oscillations [17] within the dimple flow could be investigated and approved experimentally (see, for example, [16]), as numerically using highly resolved LES [17] for dimple depth to dimple diameter ratios of  $t/D = 0.261$  and larger. In contrast to experimental observations and LES results, the asymmetric vortex structures obtained from URANS are steady and predict only one of the two extreme vortex positions ( $\alpha = \pm 45^\circ$ ) in the time-

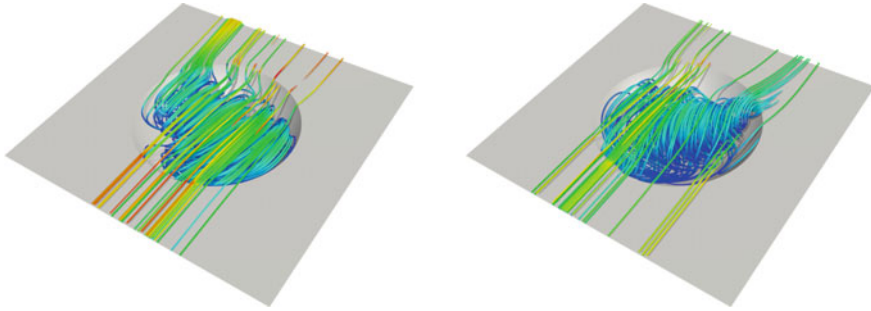


**Fig. 5** Different orientations ( $\alpha = \pm 45^\circ$ ) of the oscillating vortex structures inside the spherical dimple for  $Re_D = 42,000$

averaged flow pattern, which switch in reality almost periodically in reality. It is assumed that the self-sustained oscillations and periodic outbursts due to unsteady asymmetric vortex structures could endorse a possible self-cleaning process inside the spherical dimple and at the lower channel wall downstream of the trailing edge. Thus, LES is chosen to simulate the particulate fouling and to investigate its influence on heat transfer and friction loss for a smooth channel with a spherical dimple or square cavity.

### 3.2 Particulate Fouling on Structured Heat Transfer Surfaces

To investigate the influence of particulate fouling on the friction/pressure loss and heat transfer, a series of LES using injected particle masses up to  $m_p \approx 5.5 \text{ g/s}$  are carried out for a smooth channel with a single spherical dimple or square cavity ( $t/D = 0.261$ ,  $Re_D = 42,000$ ). Due to the results given in Fig. 4, a medium grid resolutions with around  $1.6 \times 10^6$  cells seems to be sufficient to capture the mean velocity profiles, as well as the Reynolds stresses accurate enough and is chosen for the simulation of particulate fouling. The pressure loss due to friction is expressed in terms of the skin friction factor

$$C_f = \frac{\tau_w}{\frac{1}{2}\rho_f U_b^2}, \quad (31)$$

with the shear stress  $\tau_w$ , the density of the fluid  $\rho_f$  and the bulk velocity  $U_b$  of the fluid. It should be noted that Eq. (31) has to be extended for further investigations to allow for consideration of the form drag due to structured surfaces. The heat transfer is evaluated using the Nusselt number

$$Nu = \frac{hL}{\lambda}, \quad (32)$$

where  $h$  is the convective heat transfer coefficient of the flow,  $L$  is the characteristic length ( $L$  is set to  $2H$  due to periodic boundary conditions in the streamwise direction) and  $\lambda$  is the thermal conductivity of the fluid. The Nusselt number relates the total heat transfer to the conductive heat transfer. The friction coefficient and Nusselt number received from the fouling simulations are divided by the ones obtained from a turbulent channel flow without particulate fouling, which directly expresses the increase or decrease of pressure loss and heat transfer. Therefore, the friction coefficient  $C_{f0}$  and the Nusselt number  $Nu_0$  of the smooth channel are determined using the correlations of Petukhov and Gnielinski for turbulent channel flows ( $1500 < Re_H < 2.5 \times 10^6$ ):

$$C_{f0} = (1.58 \ln(Re_H) - 2.185)^{-2}, \tag{33}$$

$$Nu_0 = \frac{(C_{f0}/2) (Re_H - 500) Pr}{1 + 12.7 (C_{f0}/2)^{1/2} (Pr^{2/3} - 1)}. \tag{34}$$

The original correlations (see [18]) are in terms of the Reynolds number  $Re_{D_h}$  based on the hydraulic diameter, but they are used in a rewritten form assuming  $D_h = 2H$  for a smooth, infinitely wide channel. Figure 6 shows the space- and time-averaged friction coefficient  $\overline{\overline{C_f}}/C_{f0}$  and Nusselt number  $\overline{\overline{Nu}}/Nu_0$  for a spherical dimple and square cavity after 30 s of physical real time, whereby no particles are considered (I) or a particle mass of  $m_p \approx 2.2$  g/s (II) or  $m_p \approx 5.5$  g/s (III) is injected. It can be seen, that the pressure loss is increased by around 29% in the case of the clean spherical dimple and approximately 61% for the clean square cavity compared to the turbulent channel flow, whereas the heat transfer is enhanced by circa 32% for the spherical dimple and 27% in the case of the square cavity. The thermo-

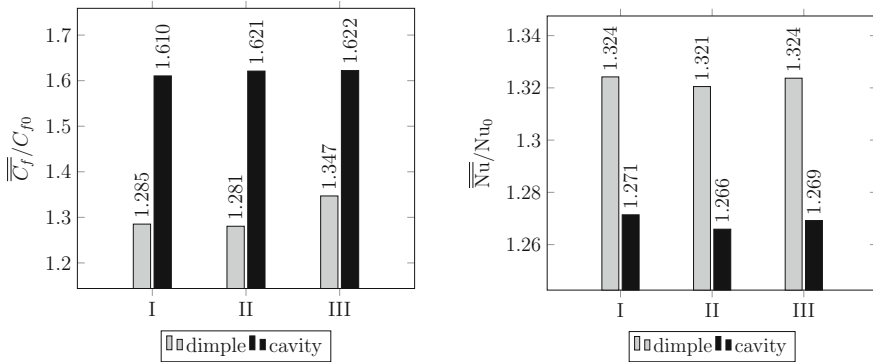


**Fig. 6** Comparison of the space- and time-averaged friction coefficient  $\overline{\overline{C_f}}/C_{f0}$  and Nusselt number  $\overline{\overline{Nu}}/Nu_0$  for a spherical dimple and square cavity after 30 s of physical real time: (I) clean surface (no particle injection), (II) particle mass injection:  $m_p \approx 2.2$  g/s, and (III) particle mass injection:  $m_p \approx 5.5$  g/s

hydraulic efficiency  $\overline{\text{Nu}}/\text{Nu}_0/(\overline{C_f}/C_{f0})^{1/3}$  achieved for the dimple is 1.22, and 1.08 for the cavity. Thus, the clean spherical dimple shows great advantages compared to the clean square cavity. In contrast, the change of pressure loss and heat transfer due to particulate fouling after 30 s of physical real time is less unambiguous. The increase of the pressure loss  $\overline{C_f}/C_{f0}$  ranges between 0.4 % (II) and 6% (III) for the spherical dimple and between 1.1% (II) and 0.1% (III) in the case of the square cavity. The decrease in the heat transfer is even smaller, varying between 0.3 and 0.6%, whereas the spherical dimple shows a slightly better fouling performance. Finally, Fig. 7 presents the total fouling layer height  $h_f$  and the total height  $h_r$  of the removed fouling layer for the spherical dimple and square cavity after 30 s of simulated physical real time for an injected particle mass of  $m_p \approx 2.2$  g/s. A relatively high particle deposition can be observed within the recirculation zone of the spherical dimple, whereas no particulate fouling is detected in the lee side of the dimple where the reattachment point lies. Due to the switching of asymmetric vortex structures and vortex outbursts (see Sect. 3.1.2), a high fouling removal rate is obtained within the lee side, and additionally downstream of the dimple's trailing edge. Moreover, due to the flow acceleration in front of the dimple, no fouling can be observed in the area

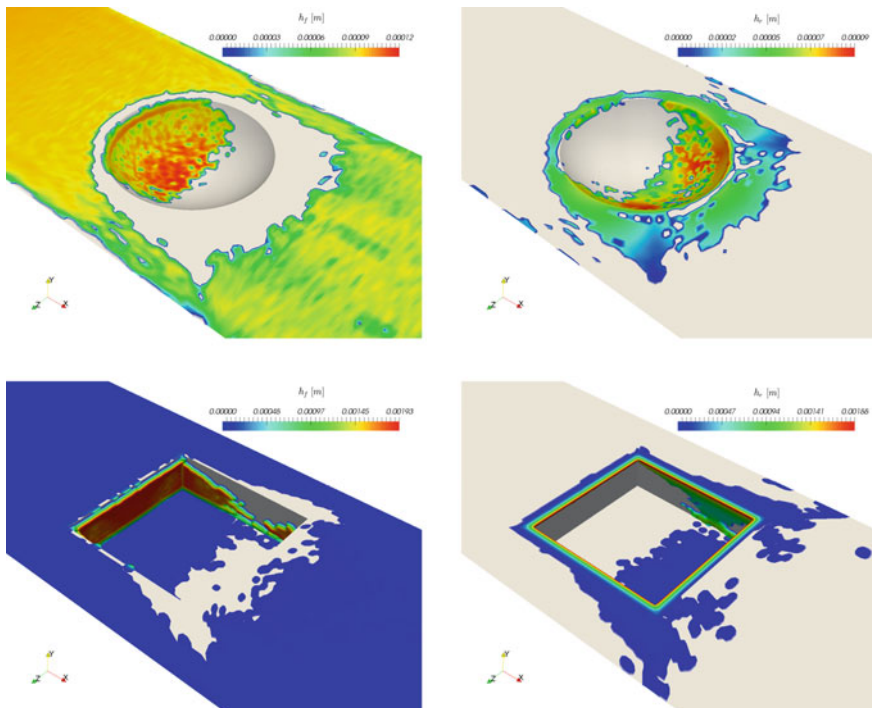


**Fig. 7** Height of the settled  $h_f$  and removed  $h_r$  fouling layer after 30 s of physical real time for an injected particle mass  $m_p \approx 2.2$  g/s: spherical dimple (left), square cavity (right)

of the dimple's front edge. The highest removal rates are obtained at both extreme positions of the asymmetric vortex structures ( $\alpha = \pm 45$ ). In the case of the square cavity, the highest particle deposition rates are gained at the vertical front side and side faces of the cavity due to adhesion, whereas the clean area downstream of the cavity's trailing edge is significantly smaller compared to the spherical dimple. More detailed investigations of the fouling mechanisms (deposition and removal) under consideration of local vortex structures using vortex identification methods will be a primary part of the next work.

## 4 Conclusion

A new multiphase method for the numerical simulation of particulate fouling processes on structured heat transfer surfaces is introduced and described in detail. A verification and validation of the LPT is carried out using the two-dimensional Taylor–Green vortex. The investigation of the flow inside a smooth channel with a spherical dimple ( $t/D = 0.261$ ,  $Re_D = 42,000$ ) confirms unsteady asymmetric vortex structures inside the dimple in the case of LES, which are primarily responsible for a self-cleaning process, respectively for the better fouling performance, in comparison to the square cavity. One of the main advantages of our new multiphase approach is the fairly low computational effort due to phase conversion and particle deletion. In addition to that, solution of an advection/transport equation for the fouling phase and costly remeshing procedures are not required, which allows for the usage of the proposed method for a general prediction of particulate fouling on structured heat transfer surfaces.

**Acknowledgements** The authors would like to thank the German Research Foundation (DFG, grant KO 3394/10-1 and INST 264/113-1 FUGG) and the North-German Supercomputing Alliance (HLRN) for supporting this work.

## References

1. P. Ligrani, *International Journal of Rotating Machinery* **2013**, 32 (2013)
2. H. Mueller-Steinhagen, *Heat Transfer Eng.* **32**, 1 (2013)
3. M. Sommerfeld, *Particle Motion in Fluids - VDI Heat Atlas* (Springer, 2010)
4. T.C. Crow, J.D. Schwarzkopf, M. Sommerfeld, Y. Tsuji, *Multiphase flows with droplets and particles*, 2nd edn. (CRC Press, Taylor & Francis, 2011)
5. A. Putnam, *ARS Journal* **31**, 1467 (1961)
6. P.G. Saffman, *J. Fluid Mech.* **22**, 385 (1965)
7. P.G. Saffman, *J. Fluid Mech.* **31**, 624 (1968)
8. R. Mei, *Int. J. Multiphase Flow* **18**, 145 (1992)
9. F. Loeffler, W. Muhr, *Chem. Ing. Tech.* **44**, 510 (1972)
10. E. Heinl, M. Bohnet, *Powder Technol.* **159**, 95 (2005)
11. A. Yoshizawa, K. Horiuti, *J. Phys. Soc. Jpn.* **54**, 2834 (1985)
12. W. Kim, S. Menon, in *AIAA, Aerospace Sciences Meeting and Exhibit, 33 rd, Reno, NV* (1995)



13. M. Germano, U. Piomelli, P. Moin, W.H. Cabot, *Phys. Fluids* **3**, 1760 (1991)
14. R. Bloechl, H. Mueller-Steinhagen, *The Canadian Journal of Chemical Engineering* **68**, 585 (1990)
15. S. Wetchagarun, A numerical study of turbulent two-phase flows. Ph.D. thesis, University of Washington (2008)
16. V.I. Terekhov, S.V. Kalinina, Y.M. Mshvidobadse, *Journal of Enhanced Heat Transfer* **4**, 131 (1997)
17. J. Turnow, N. Kornev, S. Isaev, E. Hassel, *Heat Mass Transfer*. **47**, 301 (2011)
18. M.A. Elyyan, A. Rozati, D.K. Tafti, *Int. J. Heat Mass Transfer* **51**, 2950 (2007)